minerals

MDPI

Article

Allanite in Variscan Post-Collisional Lamprophyre Dykes from Les Guilleries (NE Iberia) as a Part of Rare Earth Elements Recycling in Collisional Orogens

Esteban Mellado [1,*], Mercè Corbella [1] and Andrew Kylander-Clark [2]

[1] Department of Geology, Universitat Autònoma de Barcelona, Edifici Cs, 08193 Bellaterra, Spain; merce.corbella@uab.cat
[2] Department of Earth Science, University of California, Santa Barbara, CA 93106, USA; kylander@geol.ucsb.edu
[*] Correspondence: esteban.mellado@uab.cat

Abstract: Recent studies of Late Permian calc-alkaline lamprophyre dykes located in the Les Guilleries Paleozoic massif of the Catalan Coastal Range have revealed that allanite is present as the main REE-bearing accessory phase, which is the object of this study. The lamprophyre dykes are amphibole–plagioclase-dominated spessartites with a wide variety of accessory phases, including titanite, ilmenite, allanite, fluorapatite, spinel, zircon, and sulfides, and show complex alteration textures related to secondary albite, chlorite, epidote, titanite and calcite. The allanite crystal composition, analyzed by SEM-EPMA and LA-ICP-MS, evidences the solid solution between epidote and allanite with a ferriallanite component, similar to what is found in Variscan post-collisional granitoids from western Europe. However, heterogeneity in crystal shapes, sizes, type of zoning, dissolution embayment textures, growth of epidote coronas, mineral paragenesis, and the unique geochemical characteristics of allanite crystals suggest multiple crystallization events. At least two types of allanite–epidote composite grains have been identified: allanite Type I, with regular allanite–epidote core-to-rim zoning and a secondary allanite rim; and allanite Type II, with anhedral allanite cores surrounded by epidote coronas. Additionally, irregular zoning, complex dissolution textures and REE redistribution suggest the occurrence of deuteric and/or post-magmatic processes, which are also common in Variscan post-collisional plutons from the Catalan Coastal Range and nearby Paleozoic massifs. Multivariate statistical analyses of major elements in allanite–epidote composite grains show a relationship between major textural and geochemical variations for three out of ten principal components, mainly related to cationic substitutions between ferriallanite-(Ce) and epidote, but also involving Mn and Ti($REE^{3+} + Fe^{2+} + Ti^{4+} + Mg^{2+} + Mn^{2+} = Al^{3+} + Ca^{2+} + Fe^{3+}$). The allanite U-Pb-Th-weighted mean age of 265 ± 15 Ma (MSWD = 0.57) is roughly similar to the age of emplacement of the lamprophyres in the upper crust in the mid–late Permian, and coincides with the period following the main tectonometamorphic and magmatic events of the post-collisional evolution in the Catalan Coastal Range. Th/U and La/Sm ratios suggest a metamorphic origin for most allanite grains, but a combination of metamorphic processes prior to partial melting, early–late magmatic crystallization, and/or post-magmatic hydrothermal processes is the most plausible explanation to account for the diversity of allanite grains in Les Guilleries lamprophyres.

Keywords: allanite; geochemistry; EPMA; calc-alkaline lamprophyre; geochemistry; Les Guilleries massif; Variscan orogeny; U-Pb ages

1. Introduction

Allanite-bearing calc-alkaline lamprophyres are widespread in the Variscan Belt of western Europe [1–4] and generally represent low-volume pulses of mantle-derived mafic magmas variably enriched in LILEs, HFSEs, and REEs, and emplaced in the brittle upper crust as dyke swarms during post-collisional periods of the Variscan orogeny, unlike

Permian and Cretaceous alkaline lamprophyre dykes that are post-Variscan. While the relative abundance of amphibole–phlogopite vs. plagioclase–K-feldspar is used to classify calc-alkaline lamprophyres and is thus the usual object of studies [5], the diversity of accessory phases present in these rocks is poorly constrained. Many studies of Variscan calc-alkaline lamprophyres have reported the presence of allanite as the main REE-bearing phase [2–4], but little information about their morphology, geochemistry and geochronology has been provided. Recent studies of post-collisional Variscan spessartite dykes in the Les Guilleries massif (Catalan Coastal Range, NE Iberia) have identified allanite as the main REE-carrier phase [6].

Allanite is a member of the epidote group, and its structure can accommodate large quantities of many chemical elements, mainly depending on the system composition rather than on the P-T conditions. This mineral testifies to the diversity of mineral formation environments, as well as to secondary processes such as metamictization and hydrothermal alteration [7,8]. Allanite's simplified crystal formula is $A_2M_3(SiO_4)(Si_2O_7)O(OH)$, where the A sites are mainly occupied by Ca^{2+} and REE^{3+}, and M sites are mainly occupied by Al^{3+}, Fe^{3+}, Fe^{2+}, Mg^{2+}, $Mn^{2+,3+}$, Ti^{4+}, and Th^{4+} [8,9]. Solid ferriallanite–allanite–epidote–clinozoisite solid solutions are well known within many igneous, metamorphic and sedimentary rocks, and, as they can also be an important repository of Th and U, which makes them a promising object for U-Pb-Th dating [10]. Allanite composition varies in terms of the ratio $Fe^{3+}/(Fe^{3+} + Al)$ but is limited by whole-rock composition, so that epidote group minerals in metabasite lithologies are more Fe-rich than those in metasedimentary lithologies, which tend to be more Al-rich and typically include zoisite [11]. Slow rates of intra-crystalline Fe^{3+}-Al exchange, especially at low temperatures, preserve complex zonation patterns in individual grains that can serve as a recorders of continuous or discontinuous prograde and retrograde reactions and the P-T-fluid-redox conditions of metamorphism [11]. Allanite can exhibit a large variety of textures depending on the reaction history during metamorphism [12–14]. The transformation of allanite to monazite during low-to-medium-grade metamorphism is relatively well known [15]. Allanite commonly forms at the expense of detrital, magmatic, or metamorphic monazite close to the biotite-in reaction, at the transition between the chlorite and biotite zones [13,14,16]; allanite is consumed to form monazite during the staurolite-in reaction, at the transition between the garnet and the staurolite–kyanite zones [14,16]. Thermodynamic modelling in schists shows that the first metamorphic allanite appears at ~425 °C and 4.5 kbar, and transforms to monazite at ~600 °C and 7.5 kbar [16]. The paragenesis allanite+apatite forms during retrograde metamorphism at the expense of monazite via fluid-assisted dissolution-precipitation processes at greenschist facies [17], commonly related to shear zones [13,18].

REE-zoning in igneous allanite has long been recognized as reflecting fractional crystallization [19], most commonly from melts of high water content [20]. Experimental data on igneous allanite solubility [21,22] cover a range of melt compositions and pressures. Where allanite forms in magma, it largely controls the LREE content of the melt because it can incorporate them at weight-% level. For Th, U, and Y, as noted above, competition from coexisting phases (zircon, monazite, xenotime, titanite or rutile) may intervene. As summarized by Smye et al. [23], REE fractionation in allanite depends on magma composition. Typically, chondrite-normalized REE patterns are steeply negative for early-formed allanite, but depletion of LREEs then leads to nearly flat patterns, and the overall core-to-rim zoning in allanite may end with REE-enriched (or even REE-poor) peripheral epidote [24]. La/Sm vs. Th/U and La/Sm vs. Eu/Eu* (europium anomaly) have been used to discriminate between metamorphic and magmatic allanite, considering that fluid has lower differentiation ability for La (LREE) and Sm (MREE) than magmatic melt, whereas the mobility of U in the fluid is higher than that in the melt [25,26].

This study characterizes allanite crystals from Les Guilleries spessartite dykes (amphibole–plagioclase-dominated lamprophyres) to gain insights about their occurrence, chemical composition, age and petrogenetic implications. The presented data will be useful

for further comparison and correlation between post-collisional lamprophyre dykes of the European Variscan Belt.

2. Geological Setting

The Variscan Belt in NE Iberia is found in the Catalan Coastal Range, the Pyrenees and the Iberian Ranges. Their geology records the syn- to post-collisional magmatic evolution from peak metamorphic conditions in the Late Carboniferous [27] until the end of the orogenic cycle in the Late Permian–Triassic, which is marked by the shift from post-collisional calc-alkaline magmatism to post-orogenic alkaline magmatism [28,29]. Felsic and mafic igneous rocks of Late Carboniferous–Early Permian age and syn- to post-collisional of calc-alkaline affinity outcrop in the area. They appear to have formed from variable degrees of lower crustal assimilation and differentiation and were emplaced in the mid–upper Variscan crust in a local predominantly extensional context. They are linked to a regional dextral strike-slip regime related to late-Variscan shear zones that must have displaced Gondwana to the west with respect to Laurasia during orogenic collapse [30]. The mafic complexes are suggested to have derived from a mantle source enriched in LILEs and LREEs, attributed to metasomatic processes of the lithospheric mantle during previous subduction events [30].

In Les Guilleries Massif, located 80 km NNE of Barcelona, outcrop the oldest Variscan igneous rocks which form the Susqueda complex, the largest basic massif of the Catalan Coastal Range that intruded the Paleozoic basement. The mafic complex is composed of quartz diorites and diorites with calc-alkaline geochemical affinity, together with hornblende gabbros and hornblendites [31,32]. A syn-collisional diorite sheet has provided a U-Pb age of 323.6 ± 2.8 Ma [33] but most mafic intrusives are younger and post-tectonic [34]. Felsic rocks are younger too; leucogranites have been dated to 305–299 Ma old [33], and porphyritic granites have yielded unpublished U-Pb SHRIMP ages of 284 ± 3 Ma [35], which agrees with the age of similar mafic and felsic plutonic bodies in the nearby Montnegre Massif ($^{40}Ar/^{39}Ar$ ages between ca. 291 and 285 Ma [36]). This massif also contains ultrabasic/basic-to-intermediate rocks associated with late-Variscan calc-alkaline granites, showing mineralogical and geochemical characteristics typical of appinite suites, with cumulate hornblendites and gabbros crystalized from K-rich and fluid-rich magmas, and a complex mingled zone between diorites and biotite granodiorites [37,38].

Les Guilleries lamprophyres appear as a subvertical dyke swarm emplaced in the intersection between two perpendicular regional fault systems oriented NE–SW and NW–SE (Figure 1a,b). These dykes crosscut all previous sequences including schist and marbles from the basement and Variscan leucogranites, granodiorites, quartz-monzonites and pegmatites. The lamprophyres are porphyric to panidiomorphic spessartites, with chloritized mafic phenocrysts of different shapes and sizes between 0.5 and 1.5 mm, where amphibole is the only recognizable primary phenocrystal phase [6]. The groundmass contains mainly of chloritized and feldspathic domains (anorthite > k-feldspar), both enclosing variable proportions of amphibole (actinolite to hornblende), titanite, epidote, calcite, ilmenite, allanite, fluoroapatite, spinel, zircon, pyrite, and spinel; and variably replaced by secondary calcite, epidote, chlorite, albite, titanite and quartz. These lamprophyres present a calc-alkaline geochemical signature similar to the other igneous rocks of the area, with hybrid mantle–crust composition typical of these rocks; that is, with enrichments in MgO, Cr and Ni together with LILEs, HFSEs and REEs, and initial Sm-Nd isotopic compositions consistent with an enriched subcontinental lithospheric mantle (SCLM) source [6]. Titanite U-Pb dating yields a MSWD age of 262 ± 7 Ma, which place these dykes as the youngest calc-alkaline mafic intrusion found in the area related to the fragmentation of the Variscan Belt [6].
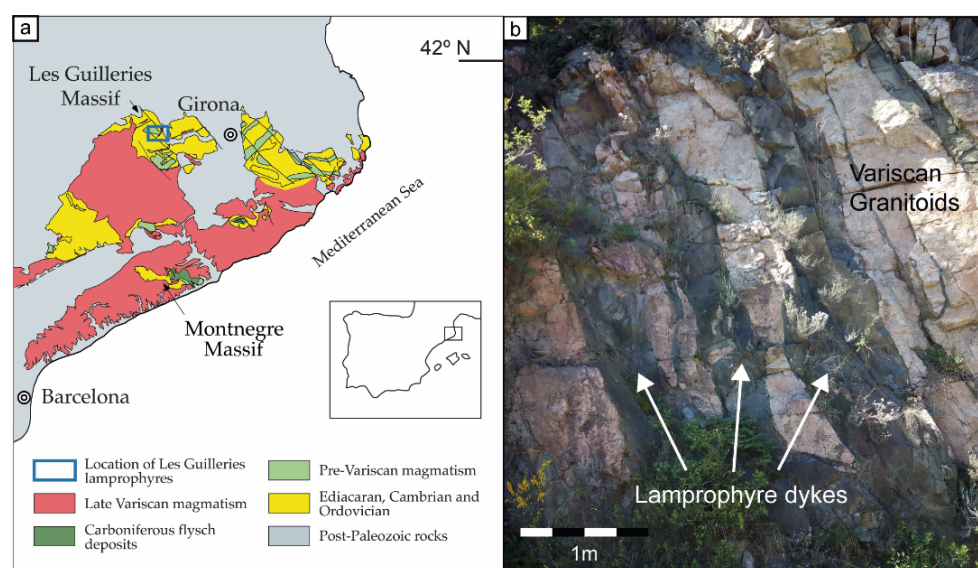
Figure 1. (**a**) Simplified geological map of the northernmost Catalan Coastal Range and geographic location of Les Guilleries massif; (**b**) Photograph of Les Guilleries spessartites dykes.

3. Materials and Methods

Petrographic analyses and SEM characterization of lamprophyre allanite crystals of 10 thin sections were performed at the Geology Department and Serveis de Microscòpia of the Universitat Autònoma de Barcelona.

The chemical composition of allanite was determined using a JEOL JXA-8230 electron microprobe at an accelerating voltage of 20 kV and a beam size of 3–5 μm at the Centres Científics i Tecnològics of the Universitat de Barcelona. Eighteen allanite crystals from two variably altered calc-alkaline lamprophyre dykes were analyzed for three different sets of elements to include Si, Ti, Al, Ca, Fe, Mg, Mn, La, Ce, Pr, Nd, Pr, Sm, Eu, Dy, Yb, Lu, Ba, Zn, Cr, V, K, Na, Th, U and F. Several elements were below detection limits: Eu to Lu (<1300 ppm), Cr < 600 ppm, V < 1000 ppm, Th and U < 2500 ppm, K < 500 ppm, Zn < 600 ppm, Na < 800 ppm, Sc < 600 ppm. SiO_2, TiO_2, Al_2O_3, CaO, FeO_{tot}, MgO, MnO, La_2O_3, Ce_2O_3, and Nd_2O_3 were analyzed in the three sets of elements.

Principal component analysis (PCA) has been used before to evaluate geochemical data [39,40]; PCA allows analysts to statistically group chemical compositions and identify possible variation trends. It is important to mention that PCA does not always represent geochemical processes, because natural geochemical processes do not always follow a multivariate Gaussian distribution or orthogonal coordinates, a prerequisite for PCA [41]. It is a useful tool to reduce bias when analyzing highly heterogeneous chemical systems and enables geological interpretations to be supported with statistics rather than stated merely as a subjective point of view. The analyses were made using scikit-learn package of Python 3.6.

In situ U-Th-Pb dating of allanite grains from two lamprophyre dykes was performed by laser-ablation split-stream ICP-MS (LASS) on the same polished thin sections used for the petrological and chemical studies. The analyses were conducted at the UC Santa Barbara (United States), following the procedures outlined in Spencer et al. [42], Kylander-Clark et al. [43], and Kylander-Clark [44]. Samples were ablated with a Photon Machines Excite 193 nm laser ablation system (San Diego, CA, USA) equipped with a HelEx cell, using a spot size of 15 μm and a repetition rate of 5 Hz. Aerosol from the laser was carried in He, mixed with Ar and analyzed by a Nu Instruments Plasma HR MC-ICPMS (Wrexham, UK) for U-Pb analysis and by an Agilent 7700X for trace element analysis. Allanite analysis and data reduction required a two-step approach, first using NIST612 glass to correct for instrument drift and bias in $^{207}Pb/^{206}Pb$ and $^{206}Pb/^{238}U$ ratios, followed by a correction of the $^{206}Pb/^{238}U$ ratio so that reference materials (RMs) SISS, BONA, and TARA yielded

ages within 2% of accepted values [23,45]. Trace elements were determined using NIST612 as the primary RM and 28Si as the internal standard, using a Si wt.% estimated by the stoichiometry of the major constituents (range of 14.9–17.3 wt.% Si).

4. Results

4.1. Petrography

Allanite is unevenly distributed within the lamprophyre matrix and is commonly found as large (10–100 micrometer) and isolated subhedral/anhedral crystals with compositions grading towards epidote, forming allanite–epidote composite grains (Figure 2). All studied grains exhibit complex growth and alteration textures, resulting in a wide variety of morphological differences. In spite of this diversity and the uniqueness of most individual composite grains, two types of morphologies are the most common. Allanite Type I corresponds to subhedral allanite cores with regular parallel zoning transitioning towards epidote rims. The zonation is perpendicular to the main crystal axis and is followed by a micrometer-size allanite outer rim (Figure 2a–c). This secondary allanite rims are not always parallel with the previous zonation (Figure 2a). Type I grains are encountered inside the feldspathic part of the lamprophyre matrix, commonly next to albitized anorthite microphenocrysts, titanite and apatite. Allanite Type II corresponds to anhedral allanite cores with irregular zoning, surrounded by epidote coronas of tens-of-micrometers thickness in sharp contact, and dissolution embayments within the allanite cores. These rounded grains are enclosed by chlorites crystals or within the chloritized part of the lamprophyre matrix, commonly next to tiny apatite crystals, euhedral amphibole, and ilmenite with titanite coronas. Type II grains are also variably replaced by secondary chlorite, albite and quartz (Figure 2d–f). Other composite grains present multiple allanite cores with apparently sigmoidal shapes (Figure 2g), while others are almost completely replaced by secondary minerals, obscuring their original morphology (Figure 2h). Additionally, some epidote coronas also show wave-like bright lines of allanite composition (Figure 2i).
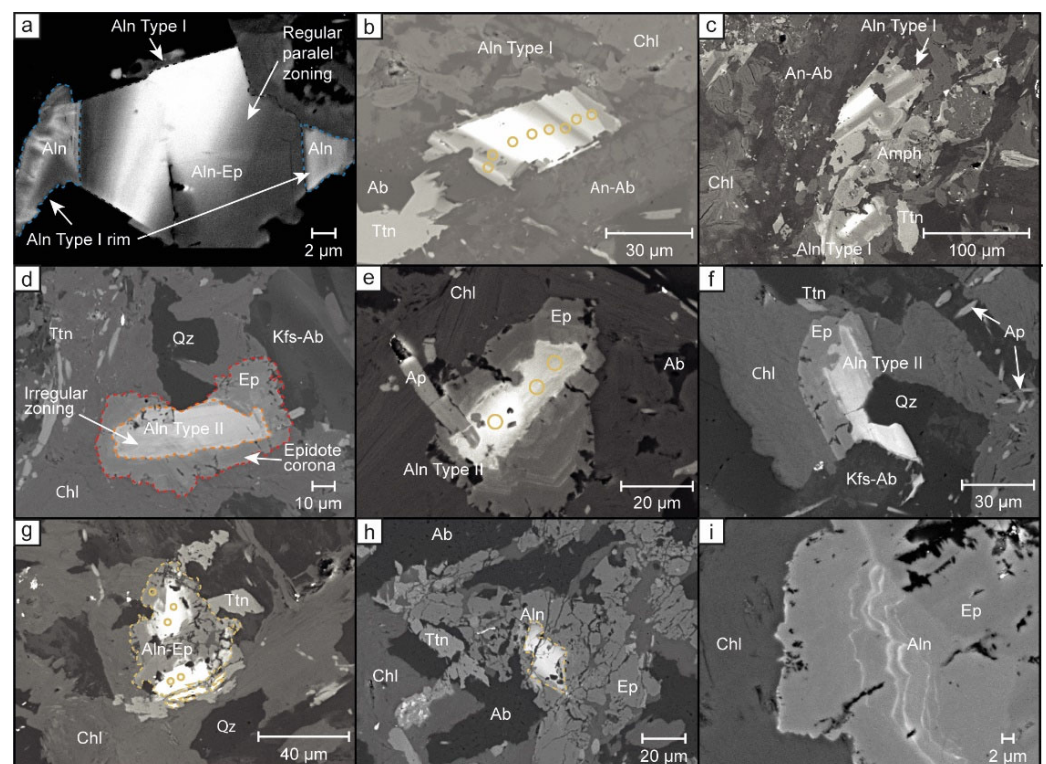

Figure 2. Back-scattered electron images representative of the morphological diversity found in allanite–epidote composite grains from Les Guilleries spessartite dykes. (**a–c**) Allanite Type I presenting

allanite cores grading towards epidote with parallel zoning and a secondary allanite rim (allanite Type I (rim)), variably affected by secondary replacement; (**d**–**f**) Allanite Type II presenting allanite cores with irregular zoning surrounded by epidote coronas, variably replaced by secondary chlorite, albite and quartz; (**g**) Unique allanite–epidote composite grain with two allanite cores and apparently sigmoidal shape in contact with titanite, surrounded by chlorite and affected by secondary albite; (**h**) Allanite fragment almost completely replaced by secondary epidote, chlorite and albite; (**i**) Wave-like allanite domain inside epidote corona. Blue, orange and red lines correspond to allanite Type I rim, allanite Type II, and epidote coronas, respectively. Yellow circles represent EPMA-analyzed spots.

4.2. Microprobe Chemistry

Electron microprobe data of 78-point analyses of 18 different allanite-epidote grains (capturing cores, zoned domains and rims) are presented in Supplementary Materials Table S1. From these analyses it is deduced that all allanite types are mainly composed of SiO_2 (30.2–38.2 wt.%), Al_2O_3 (12.8–24.3 wt.%), CaO (11.1–23.9 wt.%), FeO_{tot} (9.3–16.6 wt.%), Ce_2O_3 (0.1–11.4 wt.%), La_2O_3 (2.4–7.6 wt.%), and Nd_2O_3 (2.0–3.4 wt.%), with minimal TiO_2 (0.5–2.8 wt.%), MgO (0.2–0.7 wt.%), and MnO (0.1–0.7 wt.%). Table 1 shows a a summary of the compositional range of defined allanite types. Elemental mapping shows that the brightness in BSE images is proportional to rare earth element (Ce > La > Nd) and Fe concentration, and inversely proportional to Al, Si and Ca concentration (Figure 3).

Table 1. Range of chemical compositions obtained by EPMA of defined allanite types.

Allanite Type	Type I	Type I (rim)	Type II	Type II (EpC)	Other
N° of Analyses	24	7	21	6	20
SiO_2	30.2–38.1	33.3–36.4	30.8–35.2	37.0–38.4	30.9–37.5
Al_2O_3	13.3–24.2	20.7–24.3	12.8–22.0	23.2–24.4	13.4–22.8
CaO	11.1–23.2	15.6–21.1	11.8–19.3	22.2–23.5	11.2–21.3
FeO	10.0–15.1	9.7–10.7	10.3–15.4	11.5–12.8	10.7–16.2
Ce_2O_3	0.2–11.4	1.6–6.4	3.8–10.8	0.0–0.6	1.5–11.3
La_2O_3	0.1–7.6	0.8–4.2	2.1–5.9	0.0–0.2	0.7–7.3
Nd_2O_3	0.0–3.0	0.6–2.0	0.9–3.1	0.0–0.4	0.5–3.4
MgO	0.0–0.6	0.1–0.4	0.2–0.4	0.0–0.2	0.2–0.7
MnO	0.1–0.6	0.5–1.0	0.0–0.4	0.1–0.3	0.1–0.4
TiO_2	0.4–2.2	0.2–0.7	0.2–2.8	0.0–0.4	0.1–2.0
UO_2	<DL	<DL	<DL	<DL	<DL
ThO_2	<DL	<DL	<DL	<DL	<DL
Total	92.7–97.5	94.4–97.2	93.8–97.5	97.0–98.0	94.7–97.6
Si [apfu]	2.95–3.07	2.95–3.0	2.95–3.08	2.95–3.01	2.93–3.08
Al [apfu]	1.52–2.26	2.18–2.33	1.47–2.25	2.17–2.26	1.53–2.19
Ca [apfu]	1.15–1.97	1.48–1.84	1.23–1.75	1.89–2.0	1.15–1.86
Fe [apfu]	0.68–1.22	0.68–0.8	0.75–1.25	0.75–0.85	0.74–1.31
Ce [apfu]	0.01–0.4	0.05–0.21	0.12–0.39	0.0–0.02	0.05–0.39
La [apfu]	0.0–0.27	0.02–0.14	0.07–0.2	0.0–0.01	0.02–0.25
Nd [apfu]	0.0–0.1	0.02–0.06	0.03–0.11	0.0–0.01	0.01–0.11
Mg [apfu]	0.0–0.09	0.01–0.06	0.02–0.06	0.0–0.02	0.03–0.09
Mn [apfu]	0.0–0.04	0.04–0.07	0.0–0.03	0.01–0.02	0.01–0.03
Ti [apfu]	0.02–0.16	0.01–0.04	0.01–0.2	0.0–0.02	0.0–0.14
A	1.88–2.03	1.87–1.95	1.9–2.0	1.93–2.01	1.88–2.09
M	2.95–3.11	3.07–3.14	2.95–3.11	3.03–3.08	2.75–3.11
%Fe^{+3}	0.43–0.99	0.48–0.87	0.41–0.72	0.96–1.0	0.41–0.9
REE_2O_3 [wt.%]	0.4–22.61	2.91–13.6	7.29–20.95	0.13–1.14	2.76–21.68

Oxides in weight percent. [apfu] = atoms per formula unit. A and M correspond to crystallographic sites. REE_2O_3 = sum of rare earth element oxides. DL= detection limit.
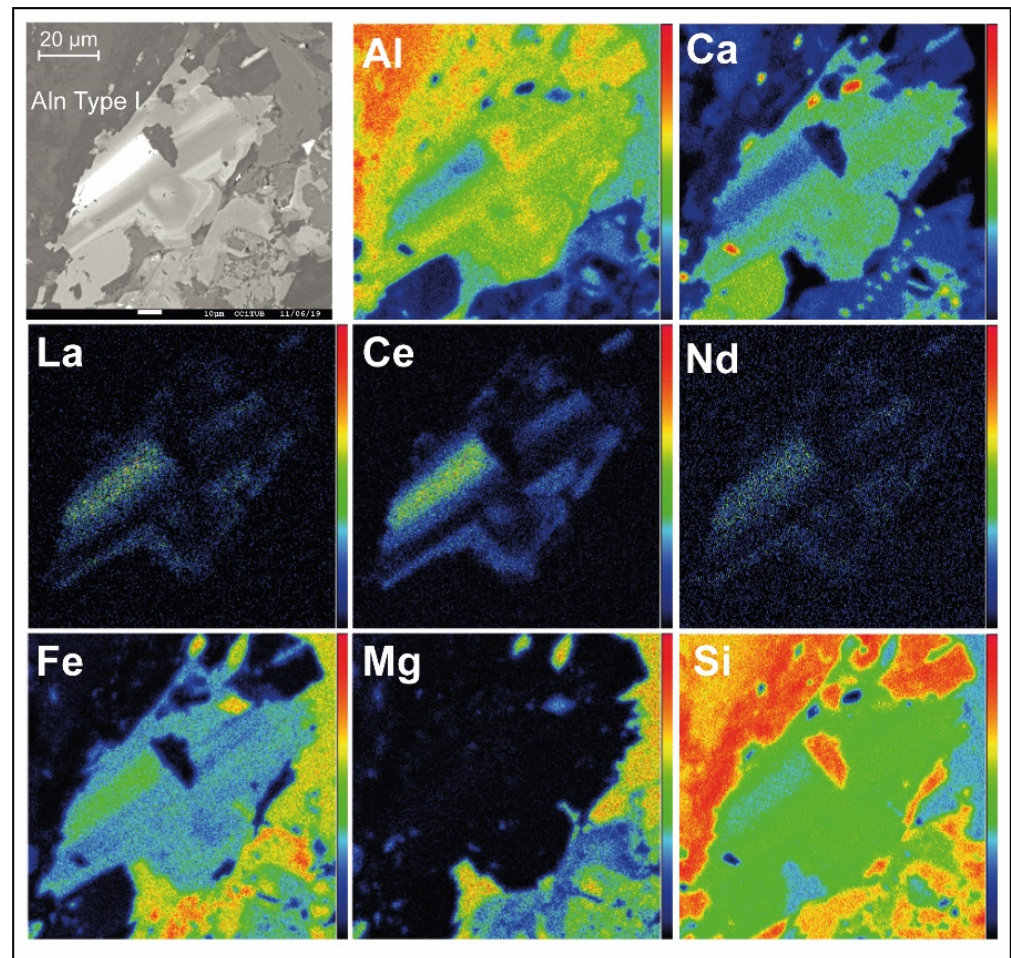
Figure 3. BSE image and concentration maps of a representative allanite Type I composite grain, including Al, Ca, La, Ce, Nd, Fe, Mg and Si. The scales for the color codes on the right-hand side of each image indicate counts of specific X-ray radiation per time unit; that is, red and yellow color indicate higher concentration, and blue-to-black the lower concentration. It is shown that the brightness of the BSE image is proportional to the REE content in allanite, which in this crystal is Ce > La > Nd.

Allanites of Type I show ferriallanite-(Ce) cores transitioning towards epidote, followed by a rim with a higher clinozoisite component and less REE enrichment (Figure 4a). Allanite Type I cores present the highest levels of REEs with a total of REE oxides up to 22.9 wt.% (Figure 4b). Type I rims have less FeO$_{tot}$ at the same level of Ce$_2$O$_3$ and more Al$_2$O$_3$ at the same level of CaO than Type I cores (Figure 4c,d). Additionally, some cores of allanite Type I present the highest MgO and lowest SiO$_2$ content compared to the rims and to allanite Type II (Figure 4e).

Allanite Type II cores show similar ferriallanite–epidote solid solution to Type I cores but with REEs never below 0.2 apfu and less REE enrichment in general when compared with Type I cores. Irregularly zoned domains in Type II present similar geochemical characteristics to parallel-zoned domains of Type I. All allanite types also show an inverse correlation between REE and SiO$_2$ content (Figure 4b).
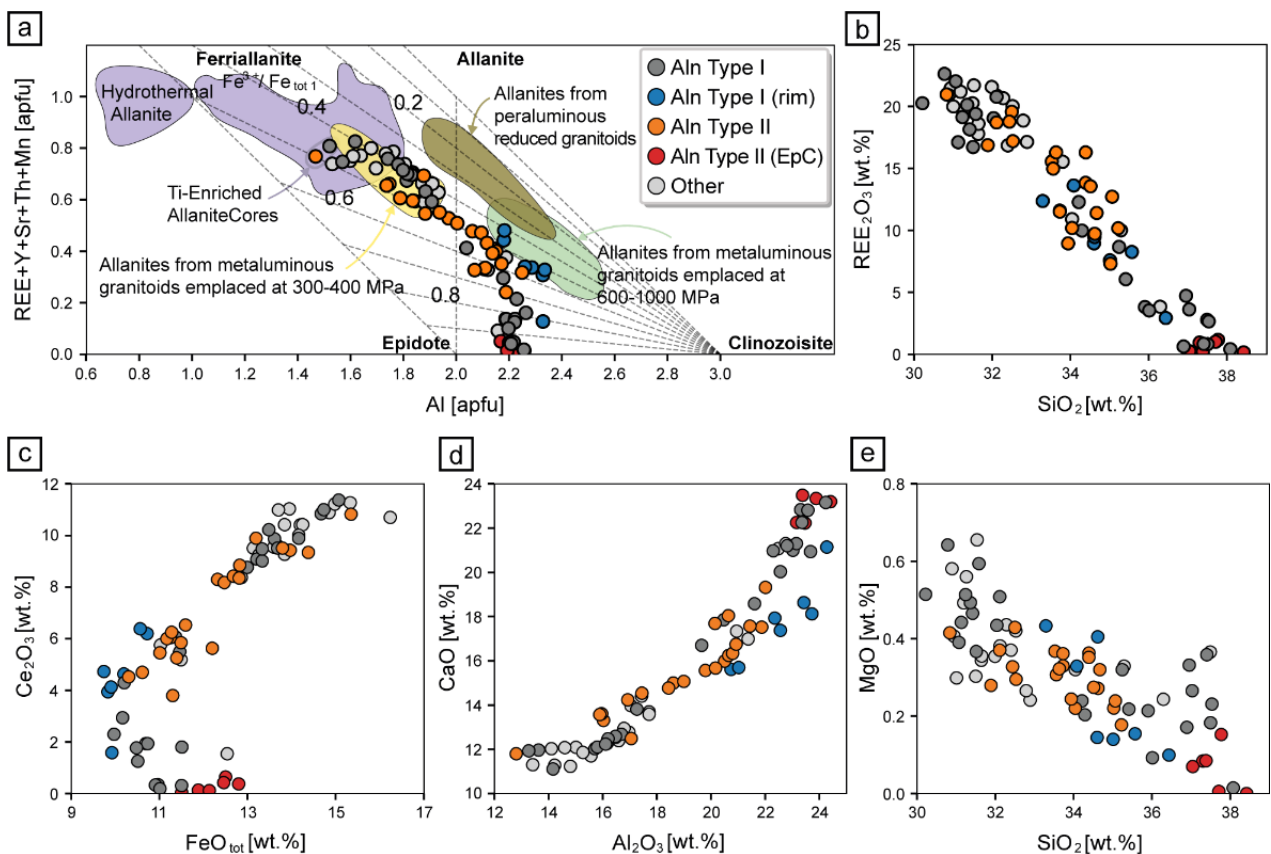
Figure 4. (**a**) Cationic Al vs. REE plot after Petrík et al. [46], showing the position of the studied allanites in the ferriallanite-allanite-epidote-clinozoisite system. (**b**) SiO_2 vs. REE_2O_3 (sum of rare earth element oxides. (**c**) FeO_{tot} (total Fe oxides) vs. Ce_2O_3. (**d**) Al_2O_3 vs. CaO. (**e**) SiO_2 vs. MgO. Aln Type I: Allanite Type I. Aln Type II: Allanite Type II. EpC: Epidote corona. Yellow, green and brown areas: allanite from peraluminous and metaluminous Variscan granitoids [47]. Purple area: hydrothermal allanite [48,49].

4.3. Principal Component Analyses

The 10 major oxides (SiO_2, Al_2O_3, CaO, FeO, Ce_2O_3, La_2O_3, Nd_2O_3, MgO, TiO_2, and MnO) of the 78 microprobe point analyses were used for PCA. The first principal component (PC1) accounts for 75.2% of the sample variance, the second principal component (PC2) accounts for 11.9%, and the third principal component (PC3) accounts for 4.8%. Accordingly, 91.9% of the variance was accounted for by the first three out of ten components (Figure 5a). This means that just three principal components describe most of the observed variation which can be visualized in binary plots. As observed in Figure 5, PC1 is dominated by the anti-correlation between Si-Al-Ca and Fe-LREE-Ti in the allanite–epidote zonation of both allanite Type I and II, while PC2 shows a relation with higher MnO values in the rims of allanite Type I. PC3 on the other hand is associated with high TiO_2 values in Type I, Type II and other allanite grains. These reveal the connection between textural and chemical variations, confirming that most of the variance of Les Guilleries lamprophyre allanites is related to the known ferriallanite–epidote solid solution (PC1), while other subtle compositional differences between cores and rims are revealed by PC2 and PC3.
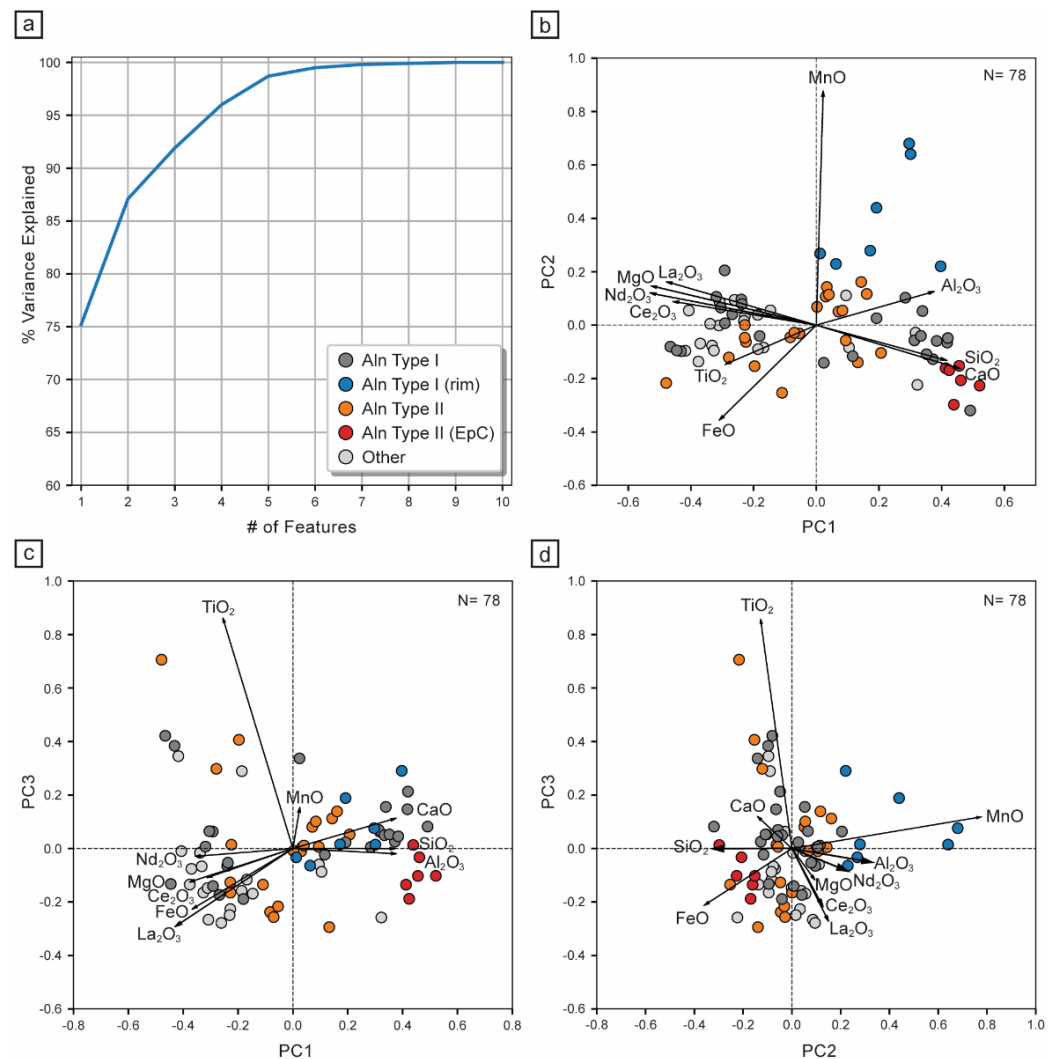
Figure 5. Principal component analysis of 10 major oxides using microprobe geochemical data. (**a**) Cumulative explained variance of the 10 principal components. A total of 91.9% of the variance is explained by the first three out of the 10 components. (**b**–**d**) correspond to binary plots of the three main principal components. (**b**) PC1 vs. PC2; (**c**) PC1 vs. PC3; (**d**) PC2 vs. PC3. The compositional vector of each major oxide is projected into principal components coordinates for easy visualization of the main patterns. N = number of point analyses considered.

4.4. LA-ICP-MS In Situ U-Th-Pb Ages

Radiometric dates obtained from 29-point analyses (Supplementary Materials Table S2) in different growth domains of five allanite crystals range between ~234–362 Ma (^{207}Pb-corrected ^{206}Pb/^{238}U date), and form a single isochron with an age of 265 ± 15 Ma (MSWD = 0.57, Figure 6); this age is equivalent to the 262 ± 7 Ma U-Pb age obtained from titanites of the same lamprophyres, interpreted as the age of lamprophyre emplacement [6]. It is important to note that the compositional changes in Type I, Type II and other allanite grains occur in a range of a few micrometers, smaller than the LA-ICP spot size of 15 micrometers, and therefore the ages obtained could represent averages of different growth domains, and not necessarily an exact period of crystal growth. Additionally, given the high uncertainty of individual allanite dates, the scatter of dates is probably the result of analytical scatter rather than geologic scatter. Nevertheless, younger dates in allanite Type I and older dates in allanite Type II are consistent with textural relationships. The rims of allanite Type I also show the youngest ages, but as they are always thinner than 5 micrometers, the dates are averaged with the internal part of the grain. On the other

hand, the timespan covered by the isochron age between ~280–250 Ma is roughly the same as the timespan covered by the late evolution of southern branch of the Variscan Belt; that is, a late Carboniferous–Permian collisional event, with localized magmatic recycling, extensional and transcurrent tectonic settings, exhumation of metamorphic terranes, and development of localized volcano-sedimentary basins [50]. The time span also corresponds to the period following the main syn- to post-collisional tectonometamorphic and magmatic evolution of the Catalan Coastal Range under the peak metamorphic conditions in Late Carboniferous described above in the Geological Setting Section, with specific periods of 305–299 Ma for leucogranites, 288 Ma for the Aiguablava pluton, and 285 Ma for porphyritic granites [33,36].
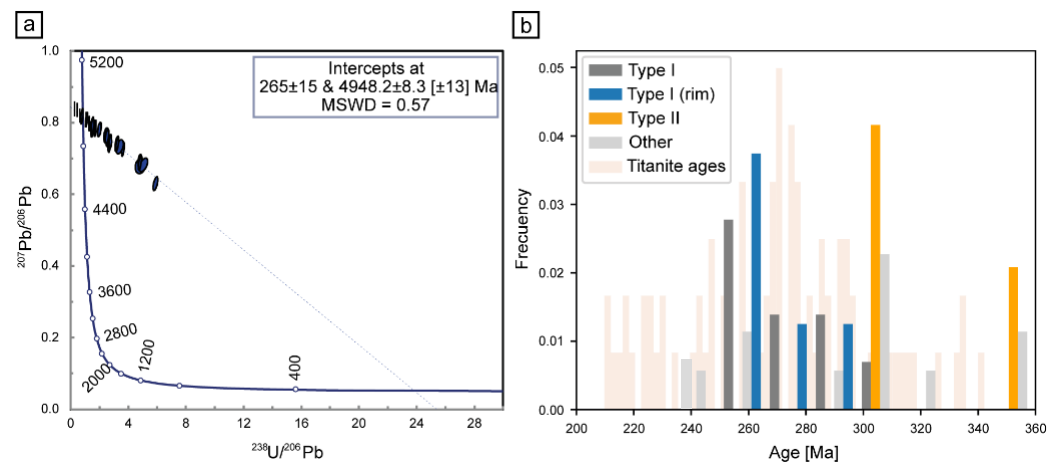

Figure 6. (**a**) Allanite Tera–Wasserburg concordia diagram using measured ^{207}Pb/^{206}Pb and ^{238}U/^{206}Pb ratios corrected for common Pb and Th content, with the data conversion performed by Isoplot 3.7. Allanite data from the two samples are plotted at 2σ and uncertainties on lower intercept ages are 95% confidence, with overall weighted average of 262 ± 7 Ma. (**b**) Histogram showing the frequency distribution of defined allanite types ranging from 234 and 362 Ma. Dated allanite crystals include the ones in Figure 2a,b,e,g. Titanite U-Pb dates from [6] are shown for comparison.

Complementary geochemical data reveal that U and Th concentrations are in the range of 4–45 ppm and 4–368 ppm, respectively (Supplementary Materials Table S2). Allanite Type I presents variable REE patterns with a tendency towards slightly-negative-to-positive Eu anomalies, decreasing Ce content, and variable trace element ratios (Figure 7). The most REE-rich cores of allanite Type I present flat HREE patterns and the highest HREE content. Allanite Type II, on the other hand, presents exclusively negative Eu anomalies, with similar HREE content in irregularly zoned cores but slightly variable LREE content, and epidote coronas with similar patterns but with total REE content lower by one order of magnitude. Th/U ratios are relatively low for all allanite types, and allanites of Type I present higher La/Sm ratios. Other allanite grains are roughly similar to allanite Type I, although unique features of some grains could also be present. Trace element ratios of all allanite–epidote grains (low Th/U and La/Sm, variable Eu/Eu*) plot in the field of metamorphic origin or closer to it in the diagram plots of La/Sm vs. Th/U and La/Sm vs. Eu/Eu* [25,26].
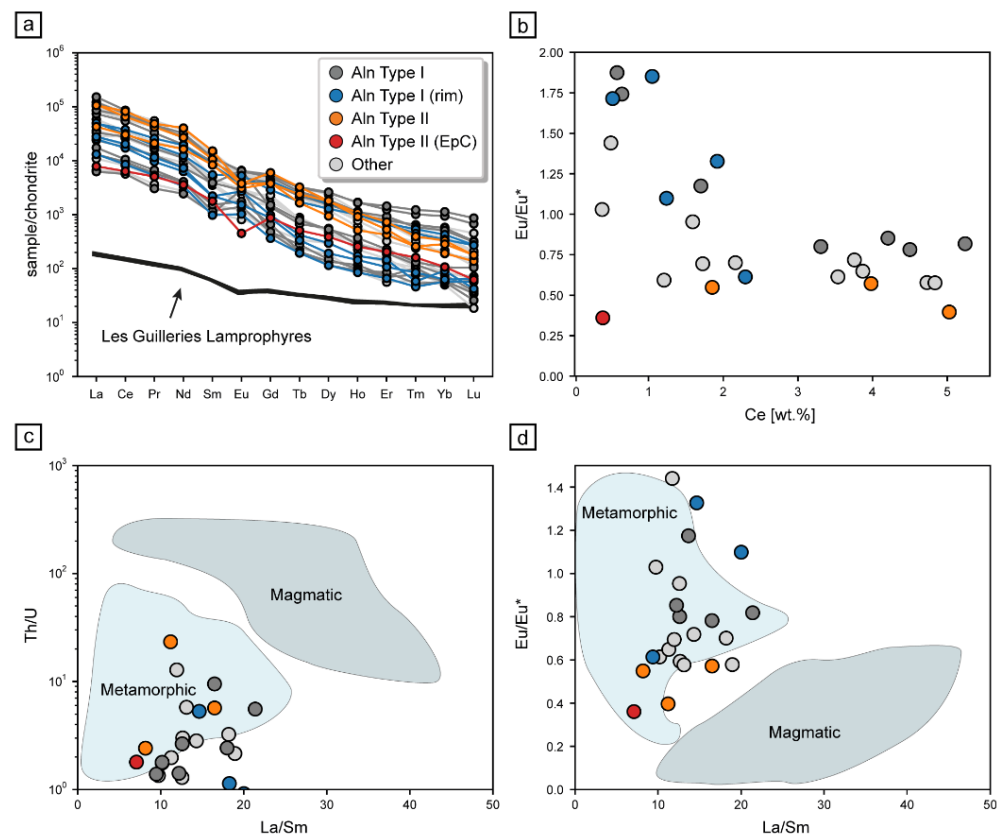
Figure 7. Trace elements of allanite from Les Guilleries lamprophyre dykes obtained by LA-ICP-MS. (**a**) Chondrite-normalized REE patterns of defined allanite types. Normalizing values are from Sun and McDonough [51]. (**b**) Ce vs. Eu/Eu* [Eu/Eu* = (Eu)cn/[(Sm)cn × (Gd)cn]0.5]. (**c**) Th/U vs. La/Sm. (**d**) Eu/Eu* vs. La/Sm. Magmatic and metamorphic allanite fields from [25,26].

5. Discussion

The textural and chemical heterogeneities of allanite–epidote composite grains found in Les Guilleries spessartite dykes suggest a complex geological story with multiple crystallization periods that could be related to metamorphic, magmatic, and/or hydrothermal processes. However, most grains are within the ferriallanite–allanite–epidote solid solution and generally present the same cationic substitutions, as indicated by PC1 of the principal component analysis, which accounts for 75% of the compositional variability (Figures 5b,c and 8a). Allanite crystals are also affected by secondary replacement, and therefore some primary features may have been modified by later processes. Nevertheless, petrographic, geochemical and statistical results show at least two distinct types of allanite–epidote composite grains. Allanite Type I, encountered in the feldspathic part of the matrix, corresponds to subhedral parallel-zoned crystals, from REE-enriched allanite cores grading towards epidote with a secondary rim of less REE-enriched allanite, the latter with a higher clinozoisite component and characteristic slight Mn enrichment, as revealed by PC2 of the principal component analysis (Figures 5b,d and 8b). Allanite Type I is apparently younger than allanite Type II and shows a variable Eu anomaly, being negative in the most REE-enriched cores, and positive towards the less REE-enriched rim (Figure 7). Allanite Type II, encountered in the chloritized part of the matrix, corresponds to REE-rich cores surrounded by epidote coronas, presents a negative Eu anomaly, and is, apparently, the oldest (Figures 6 and 7).
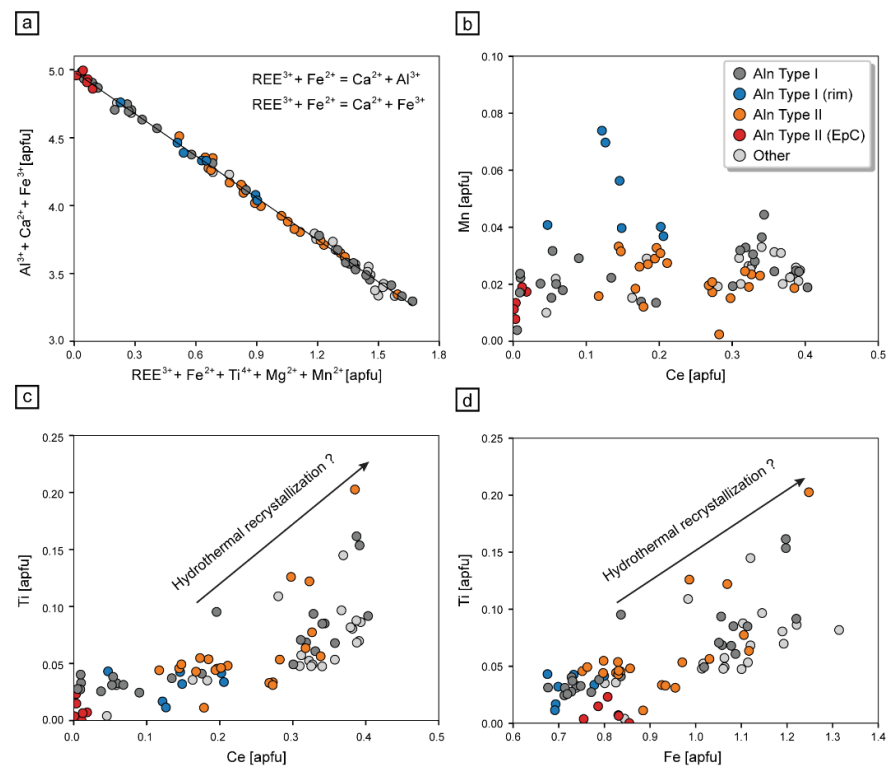
Figure 8. Cationic plots of defined allanite types relating the groups of elements resulting from the principal component analyses. (**a**) $REE^{3+} + Fe^{2+} + Ti^{4+} + Mg^{2+} + Mn^{2+}$ vs. $Al^{3+} + Ca^{2+} + Fe^{3+}$ showing the cationic substitutions in allanite structure. (**b**) Ce vs. Mn. (**c**) Ce vs. Ti. (**d**) Fe vs. Ti. [apfu] = atoms per formula unit. See explanation in the text.

Les Guilleries lamprophyres represent, to date, the last magmatic pulse with a calc-alkaline geochemical signature of the Catalan Coastal Range and Eastern Pyrenees. It occurred in a post-collisional tectonic setting related to lithospheric-scale dextral mega shear zones which developed during orogenic collapse before the onset of generalized Triassic extension [30]. These mafic dykes were emplaced in the upper Variscan crust after the main syn- to post-collisional magmatism which evolved batholitic-sized calc-alkaline granitoids, minor mafic intrusions with local ultramafic cumulates, and peraluminous leucogranite bodies. An enriched SCLM origin has been inferred indirectly for the most mafic components of the post-collisional magmatic system, and Les Guilleries lamprophyres must represent the least differentiated sample from this subduction-related enriched SCLM source [6]. According to the obtained ages, the emplacement of the lamprophyres was also cogenetic with volcanism in pull-apart basins evolving from calc-alkaline-to-alkaline geochemistry during Permian times [28] and later was affected by regional scale syn- to post-magmatic hydrothermal alteration.

Considering this interpretation, and the coincidence of allanite U-Th-Pb dates with the late Variscan evolution of the area, it is suggested that allanite crystallization was a multi-stage process related to (i) the metamorphic evolution of the SCLM source, (ii) magmatic evolution after partial melting until emplacement, (iii) deuteric/autometasomatic processes common in lamprophyres due to their high volatile content, and/or (iv) post-magmatic hydrothermal alteration. Older allanite relicts encountered in this study (allanite Type II, Figure 6) could represent unique windows to this enriched SCLM source and be a recorder of its metamorphic evolution in an environment evolving from peak compression to strike-slip motions, and of its later extension during orogenic collapse, related to mantle delamination, asthenospheric upwelling, rapid exhumation and low degree of partial melting favored by shear zones. This is supported by the similar ferriallanite–epidote composition of most allanite grains which are consistent with the nearly isochemical

evolution of a metabasic source in a nearly closed system, except for allanite Type I rims which are apparently the youngest and represent an abrupt change in thermodynamic conditions. Measured Th/La and Sm/La ratios (Figure 7c,d) are also indicative of the metamorphic origin of older grains, but we do not discount the possibility that these ratios could also be related to post-emplacement metamorphic retrogression in some of the grains, considering a rapid exhumation environment. The change from Type II to Type I allanite may also be related to a change in metamorphic conditions in the SCLM source during exhumation, or alternatively, to a change in stress conditions from dominant compression to dominant extension in the lamprophyre SCLM source. The later could explain why older allanite Type II crystals are generally rounded and anhedral while younger allanite Type I presents subhedral crystals with seemingly simple shear characteristics (Figure 2a,b). On the other hand, the unique Mn enrichment in allanite Type I rims and the higher clinozoisite component suggest a later event with a change in thermodynamic conditions that could be related to late magmatic and/or post-magmatic processes (the replacement of Mn-ilmenite by titanite as observed could be a viable mechanism to provide Mn to the system). Some unique Ti-enriched cores, revealed by PC3 of the principal component analysis, could also be associated with the latest hydrothermal processes as these are encountered in all allanite types and only in those allanite–epidote grains in which the alteration affected the internal parts of the grains (for example Figure 2f presents a high Ti core, while Figure 2d,e do not). The increase in Ti is related to increases in REEs, which suggest REEs are locally remobilized and recrystallized in hydrothermally affected cores (Figure 8c). Abundant secondary titanite suggests Ti was available during post-magmatic processes and the replacement of ilmenite by titanite—or the dissolution of Ti-rich amphiboles as observed—could be viable mechanisms to provide Ti to the system. Ti-enriched cores also present an increase in the ferriallanite component (Figure 8d), which is characteristic of hydrothermal ferriallanite [48,49]. Different concentrations of REEs, the slope and curvature in the REE patterns and the presence or absence of Eu anomalies (Figure 7) could also reflect competition between allanite and other minerals as the allanite crystals grew [15]. Therefore, the observed variations of REEs within grains and between samples may in part reflect local time-dependent changes of fluid or solid interactions of the lamprophyre magma or dykes, either in the lamprophyre's source prior to—or during—partial melting, or after consolidation in the crust.

A question remains whether the enrichment of the lamprophyre's SCLM source with rare earth elements was an ancient event that occurred before Variscan times, or whether it was the tectonic activity of the Variscan orogeny that generated lithospheric scale shear systems that allowed REE-rich fluids to penetrate the upper mantle/lower crust and crystallize as allanite in several steps during the syn- to post-collisional evolution of the mantle source. The first proposition implies the occurrence of ancient subduction-collision events, which indeed have been recorded in the area, dating from Ordovician times [52]. There is also a regional correlation in Sr and Nd isotopic compositions among the Variscan calc-alkaline lamprophyres of Western Europe that could be related to enriched mantle domains at the northern edge of Gondwana during Variscan times [6,53]. The second possibility—of a Variscan lithospheric-scale shear—implies that the oldest allanite relics could represent the beginning of the tectonic activity in the SCLM source of Les Guilleries lamprophyres during the Variscan post-collisional evolution of NE Iberia. Additionally, considering the known allanite–monazite transformations, the lack of monazite relics could also suggest a metamorphic re-equilibration of the lamprophyre's source under greenschist facies conditions after peak metamorphic conditions, consuming all monazite into allanite+apatite. Abundant apatite crystals around allanite Type I could be the result of monazite re-equilibration and dissolution. The epidote coronas around older allanite crystals (allanite Type II) may have prevented recrystallization at higher metamorphic conditions retaining previous features; therefore, it cannot be ruled out that higher metamorphic conditions were reached in the source of the lamprophyres.

Finally, it is also possible that both possibilities occurred. In this case, there would have been a recurrent recycling of rare earth elements during successive Wilson cycles, with subduction of REE-rich crustal material, REE transfer to the mantle via fluids, melts and mechanical mixing, and back up to the crust via tectonic exhumation and volcanic-magmatic systems originated from partial melting of REE-enriched mantle domains. From this discussion, it can be seen that the study of allanite crystals is a useful tool to unravel the history of deeper parts of orogenic systems.

6. Conclusions

Allanite crystals of 10–100 μm length have been identified in the matrix of late Variscan calc-alkaline lamprophyre dykes of Les Guilleries Massif (NE Variscan chain of the Iberian peninsula). Based on the complex zoning and alteration textures of the allanite crystals, two predominant types have been distinguished: Allanite Type I is found in feldspathic zones and consists of subhedral cores with regular parallel zoning that transitions smoothly into epidote; Allanite Type II corresponds to anhedral cores with irregular zoning that are in sharp contact with epidote coronas and are observed in chloritized zones. Both types show gradations from ferriallanite-(Ce) to epidote.

A principal component analysis of allanites reveals an anti-correlation between Si-Al-Ca and Fe-LREE-Ti-Mg in all grain types (PC1), which accounts for 75% of variations. PC2 relates to high concentrations of Mn in the rims of Type I, whereas PC3 is related to high Ti contents. These three principal components account for 92% of compositional differences, which can be summarized as $REE^{3+} + Fe^{2+} + Ti^{4+} + Mg^{2+} + Mn^{2+} = Al^{3+} + Ca^{2+} + Fe^{3+}$.

In situ U-Th-Pb dates of 29 analytical points in allanite crystals yield a weighted mean age of 265 ± 15 Ma. The coincidence of allanite dates in Les Guilleries lamprophyres with the period following the main syn- to post-collisional Variscan magmatism in the Catalan Coastal Range (280–250 Ma), in conjunction with the differences in allanite textures, suggest the allanite crystals from this study represent multi-stage metamorphic, magmatic and/or hydrothermal processes that occurred both before partial melting of the lamprophyre's source and later, during the early, late and post-magmatic evolution of the post-collisional system.

The low ratios of Th/U and La/Sm and variable Eu/Eu* of all analyzed allanites plot within or near the metamorphic domain. This could be due to previous ancient subduction-collision events recycling allanite, possibly in Ordovician times, or to a Variscan lithospheric-scale shear, with the oldest allanite relicts representing the beginning of the tectonic activity in the SCLM source of Les Guilleries lamprophyres (and maybe the entire Variscan collisional system of NE Iberia). In any case, recurrent recycling of rare earth elements with subduction of REE-rich crustal material into the mantle seems plausible.

Petrological, geochemical and geochronological results from this study are consistent with the interpretation that Les Guilleries lamprophyre dykes represent mantle-derived magmas that were emplaced into the brittle upper crust during late Permian times at the final stages of the Variscan orogenic collapse. This occurred in relation to shear zones, lithospheric thinning, asthenospheric upwelling, and partial melting of subduction-related enriched SCLM domains.

The Variscan basement of the Catalan Coastal Range and Eastern Pyrenees record the transition from a contractional or transpressional tectonic regime, characterized by crustal thickening, to a strike-slip regional setting that occurred during lithospheric delamination during late Variscan times, prior to the extensional collapse of the orogen and the breakup of Pangea. The results from this study suggest allanite could be a useful tool to indirectly elucidate the history of deeper parts of this system that are apparently not manifested at the surface.

References

1. Owen, J.P. Geochemistry of lamprophyres from the Western Alps, Italy: Implications for the origin of an enriched isotopic component in the Italian mantle. *Contrib. Mineral. Petrol.* **2008**, *155*, 341–362. [CrossRef]
2. Seifert, T. *Metallogeny and Petrogenesis of Lamprophyres in the Mid-European Variscides*; IOS Press: Amsterdam, The Netherlands, 2008.
3. Soder, C. Geochemistry and Petrology of Lamprophyres from the Hellenides and the European Variscides. Ph.D. Thesis, University of Heidelberg, Heidelberg, Germany, 2017.
4. Errandonea-Martin, J.; Sarrionandia, F.; Carracedo-Sánchez, M.; Gil Ibarguchi, J.I.; Eguíluz, L. Petrography and geochemistry of late- to post-Variscan vaugnerite series rocks and calc-alkaline lamprophyres within a cordierite-bearing monzogranite (the Sierra Bermeja Pluton, southern Iberian Massif). *Geol. Acta* **2018**, *16*, 237–255.
5. Le Maitre, R.; Streckeisen, A.; Zanettin, B.; Le Bas, M.; Bonin, B.; Bateman, P. (Eds.) *Igneous Rocks: A Classification and Glossary of Terms: Recommendations of the International Union of Geological Sciences Subcommission on the Systematics of Igneous Rocks*, 2nd ed.; Cambridge University Press: Cambridge, UK, 2002.
6. Mellado, E.; Corbella, M.; Navarro-Ciurana, D.; Kylander-Clark, A. The enriched Variscan lithosphere of NE Iberia: Data from post-collisional Permian calc-alkaline lamprophyre dykes of Les Guilleries. *Geol. Acta* **2021**, *19*, 1–23. [CrossRef]
7. Deer, W.A.; Howie, R.A.; Zussman, J. *Rock-Forming Minerals, Vol. 1B: Disilicates and Ringsilicates*, 2nd ed.; Longman: Harlow, UK, 1986.
8. Gieré, R.; Sorensen, S.S. Allanite and other REE-rich epidote group minerals. *Rev. Mineral. Geochem.* **2004**, *56*, 431–493. [CrossRef]
9. Armbruster, T.; Bonazzi, P.; Akasaka, M.; Bermanec, V.; Chopin, C.; Giere, R.; Heuss-Assbichler, S.; Liebscher, A.; Menchetti, S.; Pan, Y. Recommended nomenclature of epidote-group minerals. *Eur. J. Mineral.* **2006**, *18*, 551–567. [CrossRef]
10. Catlos, E.J.; Sorensen, S.S.; Harrison, T.M. Th–Pb ion-microprobe dating of allanite. *Am. Mineral.* **2000**, *85*, 633–648. [CrossRef]
11. Grapes, R.H.; Hoskin, W.O. Epidote group minerals in low-medium pressure metamorphic terranes. *Rev. Mineral. Geochem.* **2004**, *56*, 301–345. [CrossRef]
12. Finger, F.; Broska, I.; Roberts, M.P.; Schermaier, A. Replacement of primary monazite by apatite-allanite-epidote coronas in amphibolite facies granite gneiss from the eastern Alps. *Am. Mineral.* **1998**, *83*, 248–258. [CrossRef]
13. Janots, E.; Engi, M.; Berger, A.; Allaz, J.; Schwarz, J.O.; Spandler, C. Prograde metamorphic sequence of REE minerals in pelitic rocks of the Central Alps: Implications for allanite–monazite–xenotime phase relations from 250 to 610 °C. *J. Metamorph. Geol.* **2008**, *26*, 509–526. [CrossRef]
14. Janots, E.; Berger, A.; Engi, M. Physico-chemical control on the REE-mineralogy in chloritoid-grade metasediments from a single outcrop (Central Alps, Switzerland). *Lithos* **2011**, *121*, 1–11. [CrossRef]
15. Engi, M. Petrochronology based on REE-minerals: Monazite, allanite, xenotime, apatite. *Rev. Mineral. Geochem.* **2017**, *83*, 365–418. [CrossRef]
16. Goswami-Banerjee, S.; Robyr, M. Pressure and temperature conditions for crystallization of metamorphic allanite and monazite in metapelites: A case study from the Miyar Valley (high Himalayan Crystalline of Zanskar, NW India). *J. Metamorph. Geol.* **2015**, *33*, 535–556. [CrossRef]
17. Budzyń, B.; Harlov, D.; Williams, M.; Jercinovic, M. Experimental determination of stability relations between monazite, fluorapatite, allanite, and REE-epidote as a function of pressure, temperature, and fluid composition. *Am. Mineral.* **2011**, *96*, 1547–1567. [CrossRef]
18. Cenki-Tok, B.; Darling, J.; Rolland, Y.; Rossi, M.; Engi, M. Allanite Behavior in Upper-Mid Crustal Shear Zones: Can we Date Deformation Directly? Example from the Mont Blanc Massif and Implications on Its Alpine Evolution. *Terra Nova* **2011**, *0*, 1–9.
19. Levinson, A.A. A system of nomenclature for rare-earth minerals. *Am. Mineral.* **1966**, *51*, 152–158.
20. Beard, J.; Sorensen, S.; Gieré, R. REE zoning in allanite related to changing partition coefficients during crystallization: Implications for REE behaviour in an epidote-bearing tonalite. *Miner. Mag.* **2006**, *70*, 419–436. [CrossRef]

21. Klimm, K.; Blundy, J.D.; Green, T.H. Trace Element Partitioning and Accessory Phase Saturation during H$_2$O-Saturated Melting of Basalt with Implications for Subduction Zone Chemical Fluxes. *J. Petrol.* **2008**, *49*, 523–553. [CrossRef]

22. Hermann, J. Allanite: Thorium and light rare earth element carrier in subducted crust. *Chem. Geol.* **2002**, *192*, 289–306. [CrossRef]

23. Smye, A.; Roberts, N.; Condon, D.; Horstwood, M.; Parrish, R. Characterising the U-Th-Pb systematics of allanite by ID and LA-ICPMS: Implications for geochronology. *Geochim. Cosmochim. Acta* **2014**, *135*, 1–28. [CrossRef]

24. Oberli, F.; Meier, M.; Berger, A.; Rosenberg, C.; Gieré, R. U-Th-Pb and ^{230}Th/^{238}U disequilibrium isotope systematics: Precise accessory mineral chronology and melt evolution tracing in the Alpine Bergell intrusion. *Geochim. Cosmochim. Acta* **2004**, *68*, 2543–2560. [CrossRef]

25. Gregory, C.J.; Rubatto, D.; Hermann, J.; Berger, A.; Engi, M. Allanite behaviour during incipient melting in the southern Central Alps. *Geochim. Cosmochim. Acta* **2012**, *84*, 433–458. [CrossRef]

26. Janots, E.; Rubatto, D. U–Th–Pb dating of collision in the external Alpine domains (Urseren zone, Switzerland) using low temperature allanite and monazite. *Lithos* **2014**, *184–187*, 155–166. [CrossRef]

27. Reche, J.; Martínez, F.J. Evolution of bulk composition, mineralogy, strain style and fluid flow during an HT-LP metamorphic event: Sillimanite zone of the Catalan Coastal Ranges, Variscan basement, NE Iberia. *Tectonophysics* **2002**, *348*, 111–134. [CrossRef]

28. Arche, A.; López-Gómez, J. Origin of the Permian-Triassic Iberian Basin, central-eastern Spain. *Tectonophysics* **1996**, *266*, 443–464. [CrossRef]

29. Perini, G.; Cebria, J.M.; Lopez-Ruiz, J.; Doblas, M. Carboniferous-Permian mafic magmatism in the Variscan belt of Spain and France: Implications for mantle sources. *Geol. Soc. Spec. Publ.* **2004**, *223*, 415–438. [CrossRef]

30. Liesa, M.; Aguilar, C.; Castro, A.; Gisbert, G.; Reche, J.; Muñoz, J.A.; Vilà, M. The role of mantle and crust in the generation of calc-alkaline Variscan magmatism and its tectonic setting in the Eastern Pyrenees. *Lithos* **2021**, *406–407*, 106541. [CrossRef]

31. Enrique, P. The Hercynian intrusive rocks of the Catalonian Coastal Ranges (NE Spain). *Acta Geol. Hisp.* **1990**, *25*, 39–64.

32. Esteve, S.; Sunyer, J.; Culí, L.; Cirés, J.; Alías, G. El complejo intrusivo diorítico-gabroico de Susqueda (Macizo del Montseny-Guilleries, Cataluña): Unidades litológicas y características petrográficas. *Geogaceta* **2016**, *60*, 99–102.

33. Martínez, F.J.; Reche, J.; Iriondo, A. U-Pb SHRIMP-RG zircon ages of Variscan igneous rocks from the Guilleries massif (NE Iberia pre-Mesozoic basement): Geological implications. *C. R. Geosci.* **2008**, *340*, 223–232. [CrossRef]

34. Esteve, S.; Enrique, P.; Alías, G. Relaciones intrusivas y cronología relativa del plutón básico de Susqueda con las rocas metamórficas encajantes (Cordillera Prelitoral Catalana). *Geogaceta* **2018**, *63*, 107–110.

35. Martínez, F.J.; Universitat Autònoma de Barcelona, Barcelona, Spain. Personal communication, 2022.

36. Solé, J.; Cosca, M.; Sharp, Z.; Enrique, P. 40Ar/39Ar Geochronology and stable isotope geochemistry of Late-Hercynian intrusions from north-eastern Iberia with implications for argon loss in K-feldspar. *Int. J. Earth. Sci.* **2002**, *91*, 865–881.

37. Butjosa, L.; Enrique, P.; Galán, G. Las hornblenditas, gabros y dioritas del Macizo del Montnegre (Barcelona, Cordilleras Costero Catalanas). *Geogaceta* **2013**, *54*, 35–38.

38. Galán, G.; Enrique, P.; Butjosa, L.; Fernández-Roig, M. Spinels of Variscan olivine hornblendites related to the Montnegre granitoids revisited (NE Spain): Petrogenetic evidence of mafic magma mixing. *Geol. Acta* **2017**, *15*, 323–336.

39. Saxena, S.K.; Walter, L.S. A statistical-chemical and thermodynamic approach to the study of lunar mineralogy. *Geochim. Cosmochim. Acta* **1974**, *38*, 79–95. [CrossRef]

40. Ubide, T.; Gale, C.; Larrea, P.; Arranz Yagüe, E.; Lago San José, M.; Tierz, P. The Relevance of Crystal Transfer to Magma Mixing: A Case Study in Composite Dykes from the Central Pyrenees. *J. Petrol.* **2014**, *55*, 1535–1559. [CrossRef]

41. Iwamori, H.; Albarède, F. Decoupled isotopic record of ridge and subduction zone processes in oceanic basalts by independent component analysis. *Geochem. Geophys. Geosyst.* **2008**, *9*, 1525–2027. [CrossRef]

42. Spencer, K.; Hacker, B.; Kylander-Clark, A.; Andersen, T.; Cottle, J.; Stearns, M.; Poletti, J.; Seward, G. Campaign-style titanite U-Pb dating by laser-ablation ICP: Implications for crustal flow, phase transformations and titanite closure. *Chem. Geol.* **2013**, *341*, 84–101. [CrossRef]

43. Kylander-Clark, A.; Hacker, B.; Cottle, J. Laser-ablation split-stream ICP petrochronology. *Chem. Geol.* **2013**, *345*, 99–112. [CrossRef]

44. Kylander-Clark, A. Expanding Limits of Laser-Ablation U-Pb Calcite Geochronology. *Geochronology* **2020**, *2*, 343–354. [CrossRef]

45. von Blackenburg, F. Combined high-precision chronometry and geochemical tracing using accessory minerals: Applied to the Central-Alpine Bergell intrusion (central Europe). *Chem. Geol.* **1992**, *100*, 19–40. [CrossRef]

46. Petrík, I.; Broska, I.; Lipka, J.; Siman, P. Granitoid Allanite-(Ce) sub-stitution relations, redox conditions and REE distributions (on an Example of I-Type Granitoids, Western Carpathians, Slovakia). *Geol. Carpath.* **1995**, *46*, 79–94.

47. Broska, I.; Petrík, I. Accessory Phases in the Genesis of Igneous Rocks. In *Modelling of Magmatic and Allied Processes*; Kumar, S., Singh, R., Eds.; Society of Earth Scientists Series; Springer: Cham, Switzerland, 2014.

48. Vlach, S.R.F.; Gualda, G.A.R. Allanite and chevkinite in A-type granites and syenites of the Graciosa Province, southern Brazil. *Lithos* **2007**, *97*, 98–121. [CrossRef]

49. Hirtopanu, P.; Andersen, J.; Fairhurst, R.J.; Jakab, G. Allanite-(ce) and its associations, from the Ditrau alkaline intrusive massif, East Carpathians, Romania. *Proc. Rom. Acad. Series B* **2013**, *15*, 59–74.

50. Schulmann, K.; Catalán, J.R.; Lardeaux, J.; Janousek, V.; Oggiano, G. The Variscan orogeny: Extent, timescale and the formation of the European crust. In book: The Variscan Orogeny: Extent, Timescale and the Formation of the European Crust. *Geol. Soc. Spec. Publ.* **2014**, *405*, 1–6. [CrossRef]

51. Sun, S.S.; McDonough, W.F. Chemical and isotopic systematics of oceanic basalts implications for mantle composition and processes. In *Magmatism in the Ocean Basins*; Saunders, A.D., Norry, M.J., Eds.; Geological Society of London: London, UK, 1989; pp. 313–345.

52. Navidad, M.; Castiñeiras, P.; Casas, J.M.; Liesa, M.; Fernández-Suárez, J.; Barnolas, A.; Carreras, J.; Gil-Peña, I. Geochemical characterization and isotopic age of Caradocian magmatism in the northeastern Iberian Peninsula: Insights into the Late Ordovician evolution of the northern Gondwana margin. *Gondwana Res.* **2010**, *17*, 325–337. [CrossRef]

53. Dijkstra, A.H.; Hatch, C. Mapping a hidden terrane boundary in the mantle lithosphere with lamprophyres. *Nat. Commun.* **2018**, *9*, 3770. [CrossRef]